On the role of microstructural defects on precipitation, damage, and healing behavior in a novel Al-0.5Mg₂Si alloy

Ankush Kashiwar [a,b], Mariia Arseenko [a], Aude Simar [a,*], Hosni Idrissi [a,b]

[a] Institute of Mechanics, Materials and Civil Engineering (iMMC), Université catholique de Louvain, B-1348 Louvain-la-Neuve, Belgium
[b] Department of Physics, Electron Microscopy for Materials Science (EMAT), University of Antwerp, B-2020 Antwerp, Belgium

ABSTRACT

A recently developed healable Al-Mg₂Si designed by the programmed damage and repair (PDR) strategy is studied considering the role microstructural defects play on precipitation, damage, and healing. The alloy incorporates sacrificial Mg₂Si particles that precipitate after friction stir processing (FSP). They act as damage localization sites and are healable based on the solid-state diffusion of Al-matrix. A combination of different transmission electron microscopy (TEM) imaging techniques enabled the visualization and quantification of various crystallographic defects and the spatial distribution of Mg₂Si precipitates. Intragrain nucleation is found to be the dominant mechanism for precipitation during FSP whereas grain boundaries and subgrain boundaries mainly lead to coarsening of the precipitates. The statistical and spatial analyses of the damaged particles have shown particle fracture as the dominant damage mechanism which is strongly dependent on the size and aspect ratio of the particles whereas the damage was not found to depend on the location of the precipitates within the matrix. The damaged particles are associated with dislocations accumulated around them. The interplay of these dislocations is directly visualized during healing based on in situ TEM heating which revealed recovery in the matrix as an operative mechanism during the diffusion healing of the PDR alloy.

1. Introduction

Aluminum alloys are widely used as structural materials in transportation and aerospace due to their excellent combination of lightweight and strength [1]. The last five decades have witnessed significant advances in Al alloys based on our understanding of the relationships between composition, processing, microstructure, and properties [2]. The classical approach for improving the strength of Al alloys is to utilize the precipitation-hardening capability of these alloys. The strengthening by precipitation occurs as a result of the interaction of moving dislocations with precipitates during plastic deformation. The interaction is dependent on the internal stresses generated due to the misfit between precipitates and the matrix, defined by their coherency [3], and their sizes [4]. However, in general, the commercial utility of Al alloys is often adversely influenced due to the degradation of failure properties like ductility, fatigue resistance, and fracture toughness [5]. Therefore, there is tremendous scope for enhancing strength, fatigue, and damage tolerance for designing superior Al alloys with a longer lifetime.

Precipitation-strengthened Al alloys are efficiently produced by friction stir processing (FSP) and are generally known to exhibit improved mechanical properties [6,7]. Thermomechanical processing during FSP leads to microstructural homogenization together with grain refinement which occurs due to dynamic recrystallization (DRX) [7,8]. The strength and hardness are enhanced due to the combined effect of grain refinement and strengthening due to precipitates [9]. The ductility is improved due to a uniform distribution of particles, the formation of clean particle-matrix interfaces with strong interfacial bonding that are free of reactions [10], as well as elimination of large porosities or voids [11,12]. In recent efforts, Qin et al. employed FSP on Al-Mg₂Si alloys and achieved an excellent combination of hardness, ultimate tensile strength (UTS), and ductility [13]. The microstructural investigations in their study revealed an increased fraction of low-angle grain boundaries in Al-matrix from 57.7 % in the base material to 83.6 % in the nugget zone. The defects in the Al-matrix include dislocations, high-angle grain boundaries (HAGBs, misorientations > 15°), low-angle grain boundaries (LAGBs, misorientations between 5° to 15°), and subgrain boundaries (SGBs, misorientations between 2° to 5°) [14]. The interaction of these defects with the fine particles was found critical in governing the precipitation behavior and mechanical strengthening of the Al alloys [15].

Damage in Al alloys preferentially initiates on the intermetallic

particles by their fracture or matrix-interface debonding [16]. The damage mechanism involving crack initiation, growth, and coalescence is often reported to be controlled by the particle size distribution, their shapes, locations, precipitate type, and their mechanical and chemical interaction with the matrix [6,12,17]. Besides the characteristics of the particles, the strain hardening and microstructural defects as well as microstructural gradients resulting from residual stresses in the matrix significantly govern the damage evolution in Al alloys [18,19]. Now, friction stir processing has demonstrated the potential for improving the damage tolerance via breakdown of larger particles into smaller and stronger fragments, closure of the pre-existing porosity, and randomization of particle distribution [6,11,12].

Furthermore, as a step towards expanding the lifetime of Al alloys, damage management approaches like self-healing strategies have been employed. Recently, Arseenko et al. reported a novel solid-state healing strategy called Programmed Damage and Repair (PDR) which was applied to Al-0.5Mg$_2$Si alloy [20]. This strategy is based on the incorporation of damage localization particles in the matrix, where the damage is preferentially nucleated on the particles and a healing heat treatment activates diffusion in the matrix leading to the healing of cracks or voids (Fig. 1). In this Al-0.5Mg$_2$Si alloy based on the novel PDR strategy, damage is localized at Mg$_2$Si particles in a matrix with a fully precipitated microstructure. It was proposed that the Al-matrix itself acts as a source of healing which is driven by fast atomic diffusion mechanisms. The large volume fraction of crystallographic defects in the matrix including dislocations, GBs, and SGBs, act as diffusion shortcuts and enhance the diffusion rates, thereby controlling the healing potential of Al-0.5Mg$_2$Si alloy [20,21]. However, the complex interplay of these defects during damage and healing in the matrix was not fully revealed and its understanding could offer mechanistic insights into the active processes that contribute to the healing potential of PDR alloys (Fig. 1).

In the present study, the precipitation, damage, and healing behavior are investigated in the Al-0.5Mg$_2$Si PDR alloy manufactured by FSP. The mechanisms underlying the damage and healing were unveiled via in-depth microstructural investigations of the damaged submicron-sized Mg$_2$Si precipitates. Transmission electron microscopy (TEM) techniques were implemented to obtain information related to structure, crystallography, and elemental composition from micro- to atomic-scale. The healing capabilities of the alloy were demonstrated using in situ TEM heating experiments. This correlative characterization specifically aimed at the detailed understanding of the interaction of precipitates with matrix including the role of various extended crystallographic defects on the healing process.

2. Experimental and data acquisition

2.1. Materials manufacturing and testing

Al-0.5Mg$_2$Si PDR alloy samples were manufactured following the steps reported by Arseenko et al. [20]. To summarize the procedure, commercial plates of Al6063-T4 with dimensions $300 \times 70 \times 5$ mm were solution heat treated up to 525 °C followed by air cooling. Al-0.5Mg$_2$Si PDR alloy was produced by friction stir processing of Al6063-T4 plates integrating a pure Mg (>99.9 %) strip. FSP was performed using a rotational speed of 1000 rpm, traverse speed of 400 mm/min, tilt angle of 2°, pin depth of 2.8 mm, and 16 passes. A flat tensile specimen with 1 mm thickness was extracted from the nugget zone resulting from FSP, see also [20]. Damage was initiated in the specimen by the Gatan micro-test tensile machine with a maximum elongation of 0.7 mm and an applied loading rate of 0.1 mm/min.

2.2. TEM sample preparation

TEM samples were prepared from the as-FSP state before and after tensile deformation. Standard manual polishing was followed by semi-automatic polishing on 3 μm and 1 μm diamond lapping films using the MultiPrep™ polishing system to obtain specimens with a thickness of ~50 μm. Ion milling of these samples was achieved using the Gatan DuoMill 691 precision ion polishing system (PIPS) by varying the ion gun energy from 4.5 keV to 1 keV.

2.3. Microstructural characterization

The microstructural characterization was performed using different TEM imaging techniques. Bright-field TEM (BF-TEM) and dark-field TEM (DF-TEM) imaging were carried out on a ThermoFisher Tecnai G2 F20 TEM operating at 200 kV to visualize precipitates and other extended defects. Automated crystal orientation mapping in TEM (ACOM-TEM) was performed using the NanoMEGAS ASTAR system using an electron beam with a precession angle of 0.5°, a camera length of 44 mm, and a step size of 15 nm. Energy dispersive X-ray spectroscopy in scanning TEM (STEM-EDX) was conducted on a ThermoFisher Tecnai Osiris operating at 200 kV and equipped with a SuperX detector. High-
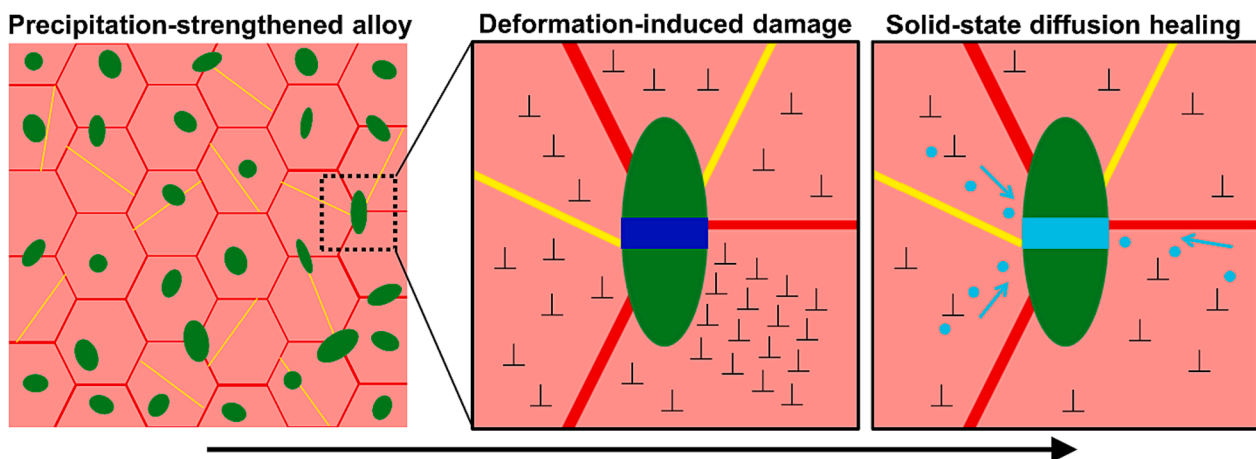
Fig. 1. Principle of the precipitation, damage, and healing mechanism in the PDR alloy which are followed sequentially with reference to the evolution of defects. GBs are in red, SGBs are in yellow and dislocations are schematized inside the matrix (light red). The matrix in the as-prepared state (after FSP) contains precipitates (in green) which lead to precipitation strengthening. Localized damage is introduced by externally applied mechanical load and indicated by a crack (in blue) inside a precipitate. Thermally activated solid-state diffusion healing is schematized by the transfer of fast-diffusing atoms (in aqua) present in the matrix towards the crack leading to its healing and the healed segment is shown in aqua. (For interpretation of the references to colour in this figure legend, the reader is referred to the web version of this article.)

resolution STEM (HRSTEM) was achieved on a ThermoFisher Titan operating at 300 kV and equipped with a probe aberration corrector and high-angle annular dark-field detector (HAADF). In situ TEM heating was performed at 350 °C for 1 min with a Gatan 652 heating holder.

2.4. Image processing

The particle size analysis of Mg_2Si particles was performed using the STEM-EDX maps obtained over several locations. For quantitative analysis, the raw maps were processed by a median filter followed by erosion, despeckle, and dilation in the ImageJ software. The particles smaller than 50 pixels (~200 nm) were excluded from the analysis. These processing steps enabled a reliable identification of most particles including the damaged or broken particles as shown in Supplementary Fig. S1.

The ACOM-TEM maps were processed using the MTEX-5.2.beta2 toolbox to analyze the GB misorientation, intragranular misorientation to mean (mis2mean) as well as kernel average misorientation (KAM). For grain identification, a segmentation angle of 2° was used whereas the KAM analysis was performed for up to 5th order neighbors with a maximum threshold angle of 2°, in order to obtain maps with reduced noise. In addition, the density of geometrically necessary dislocations (GND) was evaluated based on the Nye tensor approach using the ATEX software [22].

3. Results and discussion

3.1. Microstructural characteristics in as-FSP Al-0.5Mg₂Si alloy

Fig. 2 presents the microstructural characteristics of the Al-0.5Mg₂Si alloy in the as-FSP state. The BF-TEM image (Fig. 2(a)) shows elongated particles (pointed by red arrowheads) inside grains. These particles will be further analyzed in what follows. The grains seen in the microstructure are the result of dynamic recrystallization resulting from severe plastic deformation. Dynamic recrystallization leads to a high density of dislocation and substructures which varies between different grains. The topology of extended dislocations within a grain shows randomly arranged dislocation tangles throughout the grain indicating the activation of multiple slip systems during FSP.

Fig. 2(b) shows the crystallographic orientation of each grain observed in Fig. 2(a). They are separated by HAGBs (misorientation >15°), LAGBs (5°–15°), and SGBs (2°–5°). The region with reduced orientation reliability in grain 1 reflects the presence of the high dislocation density observable in Fig. 2(a) and the large strain that accumulated in the lattice during FSP. The polyslip occurring during FSP within the grains eventually leads to the formation of subgrains within individual grains. A subgrain 2 with a distinct diffraction contrast (Fig. 2(a)) exhibits a characteristic array of slip traces and dense walls of dislocations surrounding it (black arrows in Fig. 2(a)). This is in agreement with the presence of SGB with a small misorientation of ~3° as observed for subgrains 3 and 6. Indeed, as the SGBs and LAGBs absorb dislocations during severe plastic deformation, their misorientation increases progressively, thereby transforming them into HAGBs [23].

It is evident that although subgrain 2 shows a noticeable diffraction contrast, other grains like 3, 4, 5, and 6 do not reveal sufficient contrast changes thereby limiting the ability to identify LAGBs between these grains in the BF-TEM image. This limitation is also noticed for grains 6, 7, and 8 which exhibit larger misorientation (HAGBs). The invisibility of GBs in BF-TEM commonly arises due to the tilt conditions under which the electrons transmitting through two grains show similar diffraction contrast irrespective of their orientation. This is especially true if the GBs are edge-on or almost parallel to the electron beam as then they are unlikely to be identified. Thus, a grain analysis using ACOM-TEM with higher spatial and angular resolution becomes critical in our study for obtaining statistically relevant information on the GB characteristics, especially SGBs and small orientation gradients, that are typically seen in the microstructures after severe plastic deformation. Moreover, ACOM-TEM with a precessing nanobeam is capable of identifying the nanoscaled precipitates at any orientation, however, their reliable phase indexing is limited by the overlapping diffraction patterns from the Al-matrix. As a result, these precipitates exhibit reduced reliability and were not indexed using ACOM-TEM. They are only observed as dark particles in the inverse pole figure (IPF) map (Fig. 2(b)). In what follows, we overcome these limitations and analyze precipitation, damage, and healing behavior altogether by integrating ACOM-TEM analysis with elemental mapping using STEM-EDX.
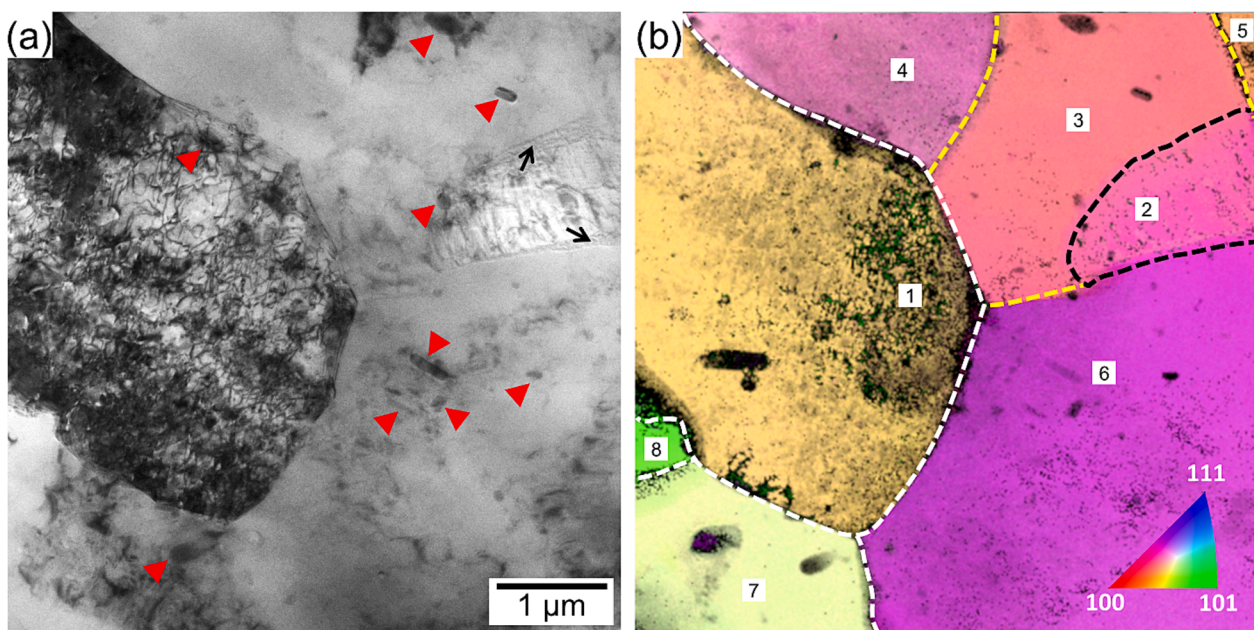
Fig. 2. Structure of Al-0.5Mg₂Si alloy in the as-FSP state: (a) BF-TEM image, (b) IPF map of the same location overlayed with cross-correlation index and reliability. HAGBs, LAGBs, and SGBs are indicated by white, yellow, and black lines, respectively. Black arrows point to dislocation walls and red triangular markers point to precipitates. (For interpretation of the references to colour in this figure legend, the reader is referred to the web version of this article.)

3.2. Precipitation behavior during FSP

The precipitation behavior was studied by considering regions with a large number of randomly distributed particles in the Al-matrix. Fig. 3 shows the results from the correlative analysis obtained using STEM-EDX, HRSTEM, and ACOM-TEM. HAADF-STEM image shows two distinct classes of particles based on the contrast sensitive to atomic number (indicated by markers in Fig. 3(a)) inside the Al-matrix (Fig. 3 (b)). Elemental maps confirm that one class of particles consists of Fe-rich intermetallic particles (Fig. 3(c)) whereas the other class is rich in Mg and Si (Fig. 3(d)-(e)). Supplementary Table S2 provides the quantitative elemental composition of the Al-matrix, Fe-rich intermetallic particles as well as Mg and Si-rich precipitates. Fig. 3(f) shows the atomic-resolution image of a Mg and Si-rich particle acquired along [1 0 0]. It confirms the presence of magnesium silicide (Mg_2Si) with two interpenetrating lattices of Mg and Si arranged in cubic anti-fluorite structure (CaF_2), with a lattice parameter equal to 6.35 Å (also shown in [24]). During FSP, the temperature of the PDR alloy reaches more than 432 °C, a temperature that favors the formation of Mg_2Si precipitates [25].

Fig. 3(g)-(i) shows the results of ACOM-TEM out of the same location as in Fig. 3(a)-(e). Fig. 3(g) shows the bright-field STEM (BF-STEM)
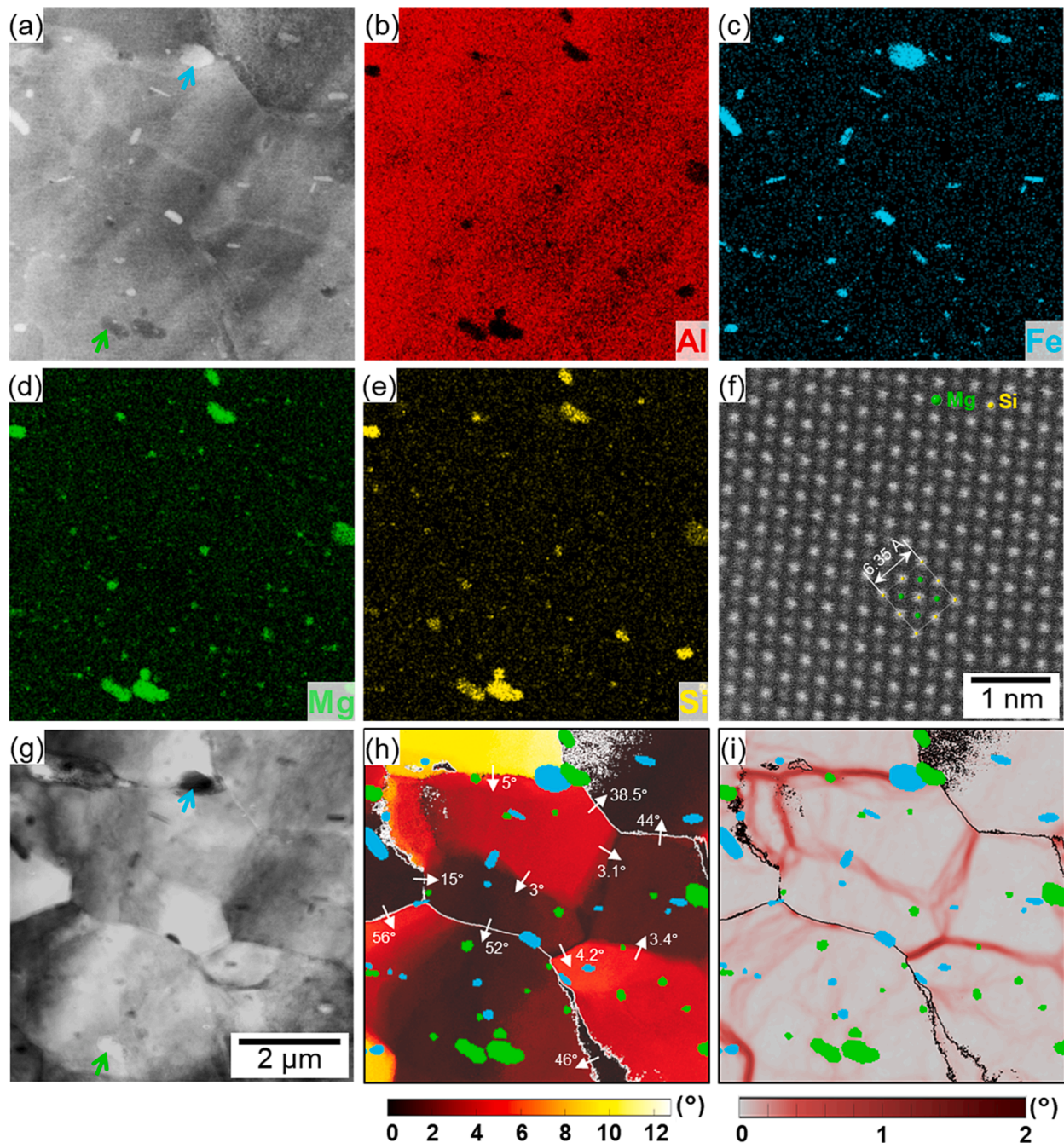
Fig. 3. Analysis of the precipitation behavior based on STEM-EDX and ACOM-TEM: (a) HAADF-STEM image with arrows showing Fe-rich intermetallic (blue) and Mg- and Si-rich particles (green), (b)-(e) elemental maps, (f) HRSTEM image of a Mg_2Si precipitate, (g) BF-STEM image with arrows showing Fe-rich intermetallic (blue) and Mg- and Si-rich particles (green) also observable in (a), (h) mis2mean map with GBs (white) with white arrows indicating misorientations at GBs and SGBs, and (i) KAM map with GBs (black) overlayed with Fe-rich (blue) and Mg-rich particles (green). The scale bar for (a)-(e) and (g)-(i) is provided in (g). (For interpretation of the references to colour in this figure legend, the reader is referred to the web version of this article.)

image with grains, subgrains, and particles. The general GBs including HAGBs and LAGBs are shown in Fig. 3(h)-(i). Although a segmentation angle of 2° was used to detect the GBs, subgrains with misorientation below 5° could not be segmented by the MTEX toolbox. Thus, in order to still visualize SGBs, we analyze the mis2mean which represents long-range (several micrometers) orientation gradients within each grain, see Fig. 3(h), whereas KAM analysis revealed the local orientation changes, see Fig. 3(i). Both the mis2mean and KAM maps are overlayed with Fe-rich intermetallics and Mg$_2$Si particles following an image processing of Fig. 3(c) and (d). From the KAM map (Fig. 3(i)), the SGBs exhibit a network of bands that separate two subgrains. The misorientations between these subgrains are less than or equal to 5° as seen in the mis2mean map (Fig. 3(h)). The SGBs are, thus, formed or associated with dense dislocation walls (DDWs) and the average thickness of these walls is equal to 222 $\pm$ 46 nm.

Fig. 3(h)-(i) also reveal the same two families of second-phase particles, Mg$_2$Si precipitates and Fe-rich intermetallics. These are mainly located within the grains and to a lesser extent at the SGBs and at GB and their triple junctions (TJ). Fe-rich intermetallics are widely investigated and known to be present in industrial Al alloys as impurities which are often reported to be sources of damage nucleation [26]. However, FSP leads to their refinement and homogenization, thereby, significantly improving the ductility of the alloys by delaying the occurrence of damage and coalescence of small internal voids [12]. However, in our Al-0.5Mg$_2$Si PDR alloy, damage nucleates first on Mg$_2$Si particles. Up to a certain strain level, Fe-rich intermetallics were observed intact by Arseenko et al. [20]. Thus, these Fe-rich intermetallic particles do not participate in the damage/healing mechanisms. In addition, their contribution to the overall strengthening of Al alloys was found insignificant [27]. As a result, the Fe-rich intermetallics are considered out of the scope of our study and will not be discussed any further.

Fig. 4(a) shows the particle size distribution of the Mg$_2$Si precipitates with a mean equivalent particle diameter of 373.8 $\pm$ 3.8 nm. The statistical analysis shows that almost all particles are smaller than 1 μm, i.e. in the sub-micrometer size range. The Feret's statistical diameter is defined as the perpendicular distance between parallel tangents touching opposite sides of the profile [28]. The mean maximum and minimum Feret's diameters were found to be 558 $\pm$ 7.4 nm and 304.3 $\pm$ 3.2 nm respectively. Fig. 4(b) shows the distribution of the Mg$_2$Si precipitates within grains and at GBs or SGBs (see also Supplementary Table S3).

Based on this statistical analysis, Mg$_2$Si precipitates can be broadly classified into two groups. The first group consists of the finest precipitates (smaller than 300 nm), that are mainly found inside grains and have an almost spherical shape (aspect ratio 1–2). Fig. 4(b) shows that more than 90 % of precipitates within the grains are of this smallest category, indicating that intragranular nucleation of Mg$_2$Si is dominating when the PDR alloy is manufactured by FSP. The second group comprises already elongated or rod-shaped (also shown in [25]) Mg$_2$Si precipitates larger than 300 nm that are found within grains and at GBs

and SGBs sites. Fig. 4(b) shows that over 30 % of the precipitates at GBs and SGBs are coarse which is comparatively higher compared to the percentage of coarse precipitates within grains (< ~ 6 %). This suggests that overall the GBs and SGBs do not act as dominant nucleation sites, however, they do promote the growth of the precipitates. Inside grains, nucleation and growth of precipitates at low or moderate temperatures are controlled by the volume diffusion assisted by vacancies [29]. At GBs, the precipitate growth is expected to occur as a sequential process: volume diffusion of solutes towards GB, GB diffusion to the precipitate site, and interfacial diffusion and deposition over the surface [30]. Both Mg and Si atoms in the highly deformed matrix are strongly accompanied by vacancies and dislocations due to steric effects [29,31]. Heating activates a flux of these defects leading to their transport towards GBs that act as sink, resulting in solute enrichment and the nucleation of precipitates at GBs [31]. Further, it is also known that GBs associated with a large fraction of defects annihilate vacancies and dislocations and act as fast diffusion pathways, thereby enhancing the precipitation and growth kinetics [32]. The precipitate growth at GBs with the large number of dislocations generated during the FSP is, thus, expected to be faster leading to the formation of coarser precipitates.

3.3. Deformation-induced damage

The damage induced by tensile deformation was accommodated by the Mg$_2$Si particles in Al-matrix, confirming that these act as damage localization sites (Fig. 5(a)) as already shown by Arseenko et al. [20]. Fracture of these particles propagates across the short axis of the Mg$_2$Si particles (Fig. 5(a)). No damage or fracture of the particles was seen in the as-prepared sample after FSP (shown in Fig. 3). Indeed, this shows that the damage is introduced during the tensile deformation of the specimen and is not an artifact of TEM specimen preparation. The particle-matrix interfaces were never found to show any sign of decohesion, suggesting that particle cracking is the principal damage mechanism in the PDR alloy. The cracking of the particles as the damage mechanism also suggests the presence of strong interfacial bonding between the particle and the matrix, which also favors mechanical strengthening in the alloy [33]. Due to the strong cohesion between particle and matrix and the mismatch in the elastic and plastic properties, the relatively softer matrix around the hard and brittle particles tends to deform under local active stresses [34].

Fig. 5(b)-(c) show complementary BF-TEM and DF-TEM of the particles and surrounding matrix that were evidenced in Fig. 5(a). An array of closely spaced dislocations (white arrows) within a deformation band are accumulating around the particles inside the matrix. This confirms the strong plastic deformation the Al-matrix underwent during tensile testing. The dislocation pile-up leads to the generation of a stress field which is sufficient to initiate damage or fracture of the particles. A general understanding of the fracture of these particles relies on the classical Griffith's criterion for fracture initiated by internal flaws [35]:
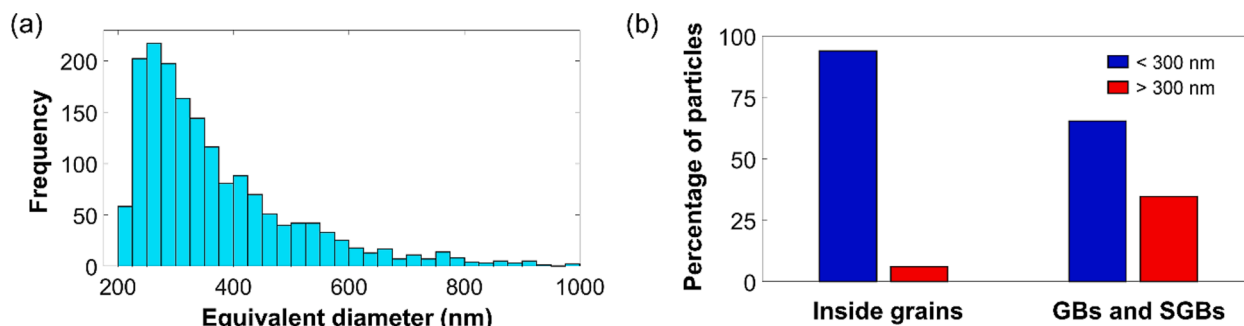
Fig. 4. (a) Particle size distribution of Mg$_2$Si precipitates analyzed from STEM-EDX mapping, (b) localization of the precipitates inside the matrix (inside grain or at GBs or SGBs) categorized into fine (<300 nm) and coarse (>300 nm), analyzed using ACOM-TEM and STEM-EDX mappings.
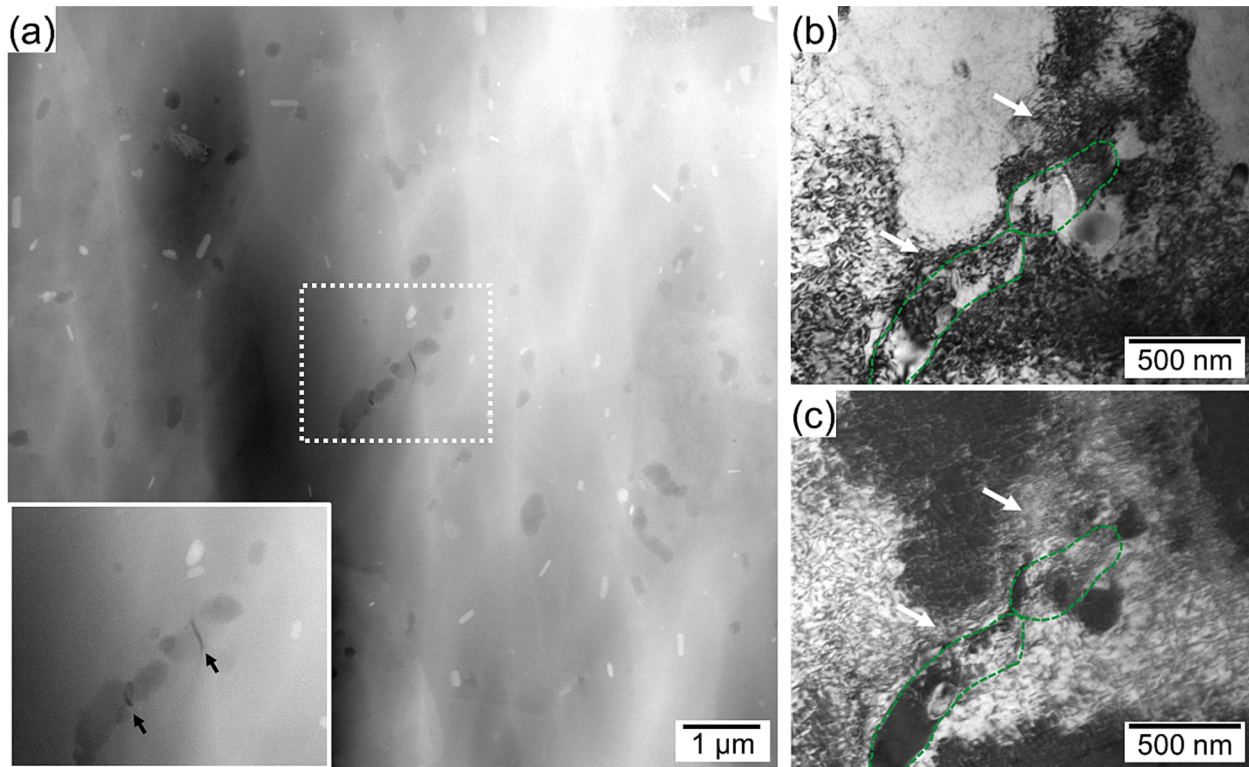
Fig. 5. (a) HAADF-STEM image showing damage indicated by arrows within dotted-box, magnified view shown in the in-set, (b) BF-TEM, and (c) DF-TEM images of cracked Mg₂Si particles seen in the box in (a), where green dotted-lines indicate particle-matrix interfaces and white arrows indicate dislocations. (For interpretation of the references to colour in this figure legend, the reader is referred to the web version of this article.)

$$\sigma_c = \sqrt{\frac{2E\gamma}{\pi C}}$$

where σ_c is the critical stress required to initiate fracture in the particle, E is the Young's modulus of the particle, γ is the surface energy and C is the length of an internal crack. The parameter 'C' is sensitive to the size of the particle. For larger particles, there is a greater probability of existence of longer cracks. Longer cracks would favor the cracking of the particles at reduced fracture stresses.

Fig. 6 displays a statistical analysis of the fractured particles based on their size, aspect ratio, and location. The figure also compares this distribution with the global analysis of all the particles, i.e. also including
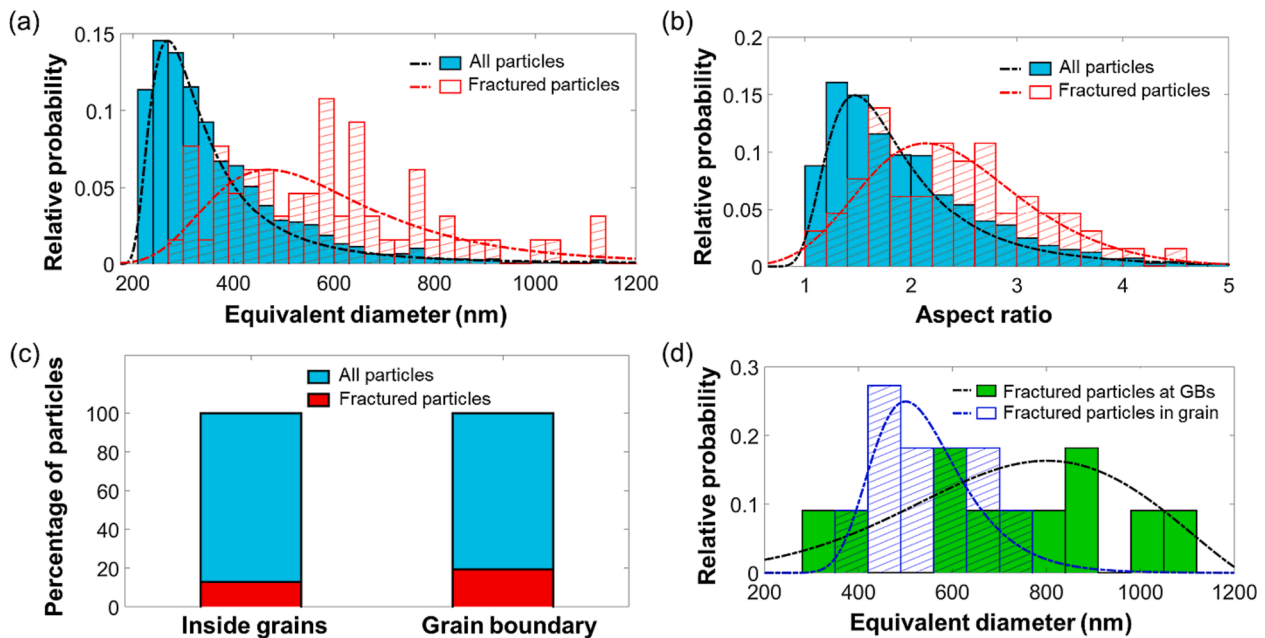
Fig. 6. Statistical analysis of the damaged particles obtained from STEM-EDX and ACOM-TEM analysis: (a) particle size distribution and (b) aspect ratio of damaged particles and all particles fitted with generalized extreme value distribution, (c) distribution of particles in grain and at GBs (HAGBs and LAGBs), and (d) size distribution of particles inside grain and at GBs (HAGBs and LAGBs) fitted with generalized extreme value distribution.

undamaged particles. The size of the damaged particles is in the range from 290 nm to 1714 nm with a mean equivalent diameter equal to 603.6 ± 30.6 nm. This size is clearly larger when compared with the mean overall precipitate size after FSP (i.e. 373.8 nm). The relative probability distribution in Fig. 6(a) shows that the size distribution of the damaged particles shifts significantly towards larger sizes, i.e. particles greater than ~ 300 nm have a higher probability of fracture. Fig. 6 (b) shows that the particles with a larger aspect ratio (over 2) have a greater probability of fracture.

Li et al. conducted a quantitative analysis that showed the sensitivity of damage in particles to various microstructural variables related to their morphology and spatial distribution [5]. Their analysis showed that relatively larger particles have greater susceptibility towards damage and generally contribute to damage localization. According to their study, it was revealed that particle size and local spatial distribution strongly affect the particle fracture whereas the particle shape (or the aspect ratio) moderately influences the damage susceptibility. In another study, by analyzing fractography results, Emamy et al. concluded that refining and increasing the roundness of the particles leads to a reduced tendency for fracture due to the reductions in sharp tips that typically act as sites with increased stress concentrations [34]. Lassance et al. also concluded that the presence of coarse and elongated particles is a key microstructural feature influencing the fracture behavior in 6xxx Al alloy [36]. From their study, as the particles converted from elongated to more round shape, the overall fracture strain improved by a factor of two at room temperature and even more at elevated temperatures.

Fig. 6(c) (see also Supplementary Table S4) shows the distribution of particles within the grains and at GBs. This gathers results for HAGBs and LAGBs. Fig. 6(c), shows that the percentage of fractured particles that are located at GBs (19.4 %) is only slightly higher compared with fractured particles that are inside grains (12.9 %). Fig. 6(d) shows that the fractured particles are mostly larger than 300 nm i.e. coarse and GBs encompass a wider size range of fractured particles compared to those within the grain. These results are in agreement with the previous statistics related to precipitation (Fig. 4(b) and Supplementary Table S3) which showed that coarser (>300 nm) and more elongated particles have a greater tendency to form at GBs than within grains. Such particles also have a greater probability of fracture, as revealed by Fig. 6(a)-(b). However, from Supplementary Table S4, it may be noted that the actual number of damaged particles seen at GBs and within grains are nearly similar. From these results, it can be concluded that both intragrain and intergranular damage localization sites are active during the plastic deformation of the PDR alloy. Thus, the size and aspect ratio of the particles are the principal parameters governing their tendency to fracture irrespective of their location.

3.4. In situ TEM observation of healing processes

The healing process was analyzed in detail for a cracked Mg_2Si particle using in situ TEM heating in combination with STEM-EDX and ACOM-TEM, see Fig. 7. In situ TEM is used for a direct correlation of the healing process with the microstructural changes in the matrix. It allowed for imaging with high spatial resolution of the localized area around a cracked particle before and after healing and to make a quantitative comparison of the microstructure under similar imaging
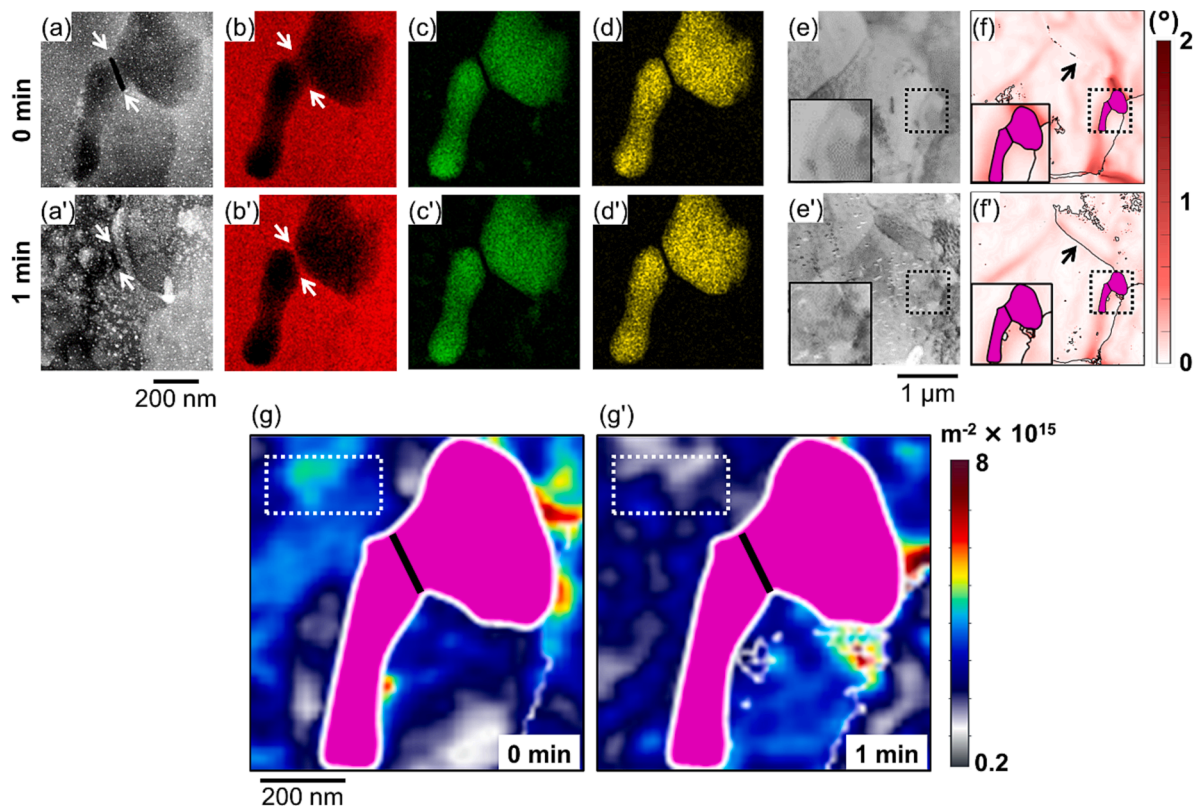
Fig. 7. Analysis of the healing process in Al-0.5Mg₂Si alloy based on in situ TEM heating in combination with STEM-EDX ((a)-(d)) and ACOM-TEM ((e)-(g)) in the initial or pre-healed state: (a) HAADF-STEM image with arrows pointing to the crack, (b) Al-map, (c) Mg-map, (d) Si-map, (e) BF-STEM with dotted-rectangle showing the exact location of acquisition of the STEM-EDX maps in (a)-(d), in-set shows magnified view of the area within the rectangle, (f) KAM map from the same region seen in (e) and overlayed with Mg₂Si particle (pink) traced as analyzed using STEM-EDX, in-set shows magnified view of area within the dotted-rectangle, and the location of crack (black segment), and (g) magnified GND map from the dotted-rectangle (in (e)-(f)) with Mg₂Si particle (pink) and the location of crack (black segment). (a')-(g') are the respective images after 1 min of healing heat treatment at 350 °C. Scale bar for (a)-(a') to (d)-(d') is shown below (a'), for (e)-(e') and (f)-(f') is shown below (e') and for (g)-(g') is shown below (g). The dotted-box in (g)-(g') indicates the region where the local GND is computed. (For interpretation of the references to colour in this figure legend, the reader is referred to the web version of this article.)

conditions. In situ TEM heating at 350 °C showed partial healing of the crack, compare Fig. 7(a) and (a'). A short heating time of 1 min was used which allowed for only partial healing. Thus, the microstructural changes that occur during the transition from the damaged to completely healed state were captured and correlated with the healing process. Elemental maps in Fig. 7(b-d) and Fig. 7(b'-d') show a sharp contrast in the Al-map due to the diffusion of Al-matrix in the healed crack. Fig. 7(e-g) and Fig. 7(e'-g') show ACOM-TEM analysis carried out for the matrix around the same particle (located within the box evidenced in Fig. 7(e-e')) in order to understand the microstructural evolution before and after healing. Fig. 7(e') shows a change of diffraction contrast in the matrix compared with the initial state (i.e. before healing), see Fig. 7(e). It indicates a change in the structure of defects as the matrix around the particle is healed. The defects' evolution is thus analyzed inside the matrix based on KAM and GND density maps. From the KAM maps in Fig. 7(f) and Fig. 7(f'), it is evident that locally the KAM around the particle in the matrix decreases during the healing. A LAGB (6°–7°) indicated by a black arrow in Fig. 7(f) transforms to a HAGB (43°) (Fig. 7(f')), leading to the formation of a triple junction exactly where the healed particle is located. The GND density maps in Fig. 7(g) and Fig. 7(g') show a reduction in the GND density in the direct vicinity of the particle, especially surrounding the interfaces through which the matrix diffuses to heal the cracks. The local GND density as computed from the area of 270 nm × 135 nm (dotted-box in Fig. 7(g)-(g')) around the healed particle-matrix interface is reduced from 2.97×10^{15} m^{-2} to 2.3×10^{15} m^{-2}. This suggests that the healing process is combined with recovery in the neighborhood of the particle. Besides recovery, it is also likely that the mobile dislocations can be absorbed by the LAGB which transforms into HAGB. This is the classical mechanism governing the transformation of subgrains into a fully recrystallized structure [23].

Healing is first expected to initiate at the crack tip as it is a region with high stress concentration and increased dislocation density (seen in the dotted-box in Fig. 7(g)) [21]. The dislocations are associated with long-range stress fields and as a result, a gradient of the equilibrium concentration of the vacancies is located around them [37,38]. At temperatures that are sufficiently high for diffusion, a flux of vacancies or atoms is generated which eventually leads to healing or annihilation of dislocations restoring the regular periodic arrangement of atoms [37]. It is the annihilation of dislocations associated with the healing of the matrix which we report here experimentally. Furthermore, the dislocations intersecting nanoscale cracks can accelerate the transport of solute atoms via pipe diffusion thereby providing directional mass transport at temperatures where volume diffusion through undisturbed solid would be too slow [39,40]. The fast-diffusing Mg atoms already present in the solid solution are strongly coupled to the vacancies and dislocations [31]. The high temperature activates the flux of these defects and the Mg atoms quickly diffuse towards the crack to reduce the interfacial energy which is followed by slower Al atoms that are expected to follow similar short-cuts until homogenization is reached, as proposed by Gheysen et al. [21].

4. Conclusion

The present work investigated the role of extended crystallographic defects and presented a statistical analysis of precipitation and damage behavior in an Al-0.5Mg$_2$Si PDR alloy manufactured by FSP. FSP resulted in the activation of multiple slip systems which eventually led to the breakdown of grains and the formation of subgrains. During FSP, Mg$_2$Si precipitated within the grains, at HAGBs, LAGBs as well as at SGBs. Fine and more round-shaped precipitates smaller than 300 nm are shown to form mainly within the grains which suggested intragranular nucleation driven by volume diffusion as a dominant mechanism. The coarser and elongated particles larger than 300 nm are mostly located at GBs and SGBs which showed that intergranular growth dominates over intragranular growth of the precipitates.

Mg$_2$Si precipitates are the only carriers of the damage and particle fracture is found to be the main damage mechanism, whereas no decohesion of the particle-matrix interfaces was evidenced. The size and aspect ratio of the precipitates are critical in controlling their cracking irrespective of their location i.e. the active damage sites are located within grains or at GBs. Based on the statistical analyses, it is thus proposed that precipitation of more regular-shaped particles and limiting the particle growth within the submicron regime are critical for improved damage tolerance of the PDR alloy. The fractured particles restrict the plastic deformation in the matrix and accumulate long-range dislocations around them which favor the healing performance of the PDR alloy. Indeed, healing is associated with the reduction of dislocation density or recovery around the particle. Now the requirement of such dislocation tangles for healing could possibly limit the capacity to apply multiple healing steps.

CRediT authorship contribution statement

Ankush Kashiwar: Conceptualization, Data curation, Formal analysis, Investigation, Methodology, Validation, Visualization, Writing – original draft. **Mariia Arseenko:** Conceptualization, Data curation, Formal analysis, Methodology, Supervision, Validation, Writing – review & editing. **Aude Simar:** Conceptualization, Formal analysis, Funding acquisition, Resources, Supervision, Writing – review & editing. **Hosni Idrissi:** Conceptualization, Formal analysis, Investigation, Supervision, Writing – review & editing.

Declaration of competing interest

The authors declare that they have no known competing financial interests or personal relationships that could have appeared to influence the work reported in this paper.

Data availability

Data will be made available on request.

Acknowledgments

Appendix A. Supplementary data

Supplementary data to this article can be found online at https://doi.org/10.1016/j.matdes.2024.112765.

References

[1] L. Stemper, M.A. Tunes, R. Tosone, P.J. Uggowitzer, S. Pogatscher, On the potential of aluminum crossover alloys, Prog. Mater. Sci. 124 (2022) 100873, https://doi.org/10.1016/J.PMATSCI.2021.100873.

[2] S.S. Li, X. Yue, Q.Y. Li, H.L. Peng, B.X. Dong, T.S. Liu, H.Y. Yang, J. Fan, S.L. Shu, F. Qiu, Q.C. Jiang, Development and applications of aluminum alloys for aerospace industry, J. Mater. Res. Technol. 27 (2023) 944–983, https://doi.org/10.1016/J.JMRT.2023.09.274.

[3] R.G. Baker, D.G. Brandon, J. Nutting, The growth of precipitates, Philos. Mag.: J. Theor. Exp. Appl. Phys. 4 (1959) 1339–1345, https://doi.org/10.1080/14786435908233369.

[4] S. Peng, Z. Wang, J. Li, Q. Fang, Y. Wei, Beyond Orowan hardening: Mapping the four distinct mechanisms associated with dislocation-precipitate interaction, Int. J. Plast. 169 (2023) 103710, https://doi.org/10.1016/J.IJPLAS.2023.103710.

[5] M. Li, S. Ghosh, O. Richmond, An experimental–computational approach to the investigation of damage evolution in discontinuously reinforced aluminum matrix composite, Acta Mater. 47 (1999) 3515–3532, https://doi.org/10.1016/S1359-6454(99)00148-2.

[6] M.B. Lezaack, F. Hannard, L. Zhao, A. Orekhov, J. Adrien, A. Miettinen, H. Idrissi, A. Simar, Towards ductilization of high strength 7XXX aluminium alloys via microstructural modifications obtained by friction stir processing and heat treatments, Materialia (Oxf.) 20 (2021) 101248, https://doi.org/10.1016/J.MTLA.2021.101248.

[7] Z.Y. Ma, A.H. Feng, D.L. Chen, J. Shen, Recent advances in friction stir welding/processing of aluminum alloys: microstructural evolution and mechanical properties, Crit. Rev. Solid State Mater. Sci. 43 (2018) 269–333, https://doi.org/10.1080/10408436.2017.1358145.

[8] A. Moharrami, A. Razaghian, M. Paidar, M. Šlapáková, O.O. Ojo, R. Taghiabadi, Enhancing the mechanical and tribological properties of Mg2Si-rich aluminum alloys by multi-pass friction stir processing, Mater. Chem. Phys. 250 (2020) 123066, https://doi.org/10.1016/J.MATCHEMPHYS.2020.123066.

[9] X. Feng, H. Liu, S. Suresh Babu, Effect of grain size refinement and precipitation reactions on strengthening in friction stir processed Al–Cu alloys, Scr. Mater. 65 (2011) 1057–1060, https://doi.org/10.1016/J.SCRIPTAMAT.2011.09.009.

[10] R. Bauri, D. Yadav, Processing Metal Matrix Composite (MMC) by FSP, in: Metal Matrix Composites by Friction Stir Processing, Elsevier, 2018: pp. 31–55. https://doi.org/10.1016/b978-0-12-813729-1.00003-6.

[11] A. Heidarzadeh, M. Khorshidi, R. Mohammadzadeh, R. Khajeh, M. Mofarrehi, M. Javidani, X.G. Chen, Multipass friction stir processing of laser-powder bed fusion AlSi10Mg: Microstructure and mechanical properties, Materials, 16 (2023) 1559. https://doi.org/10.3390/MA16041559.

[12] F. Hannard, S. Castin, E. Maire, R. Mokso, T. Pardoen, A. Simar, Ductilization of aluminium alloy 6056 by friction stir processing, Acta Mater. 130 (2017) 121–136, https://doi.org/10.1016/J.ACTAMAT.2017.01.047.

[13] Q.D. Qin, H.L. Zhao, J. Li, Y.Z. Zhang, X.D. Su, Microstructure and mechanical properties of friction stir processed Al–Mg2Si alloys, Trans. Nonferrous Met. Soc. China (Engl. Ed.) 30 (2020) 2355–2368, https://doi.org/10.1016/S1003-6326(20)65384-5.

[14] G. Huang, J. Wu, W. Hou, Y. Shen, Microstructure, mechanical properties and strengthening mechanism of titanium particle reinforced aluminum matrix composites produced by submerged friction stir processing, Mater. Sci. Eng. A 734 (2018) 353–363, https://doi.org/10.1016/J.MSEA.2018.08.015.

[15] S.C. Krishnamurthy, M. Arseenko, A. Kashiwar, P. Dufour, Y. Marchal, J. Delahaye, H. Idrissi, T. Pardoen, A. Mertens, A. Simar, Controlled precipitation in a new Al-Mg-Sc alloy for enhanced corrosion behavior while maintaining the mechanical performance, Mater. Charact. (2023) 112886, https://doi.org/10.1016/J.MATCHAR.2023.112886.

[16] M. Hu, Y. Sun, J. He, C. Li, H. Li, L. Yu, Y. Liu, Hot deformation behaviour and microstructure evolution of Al-3%Mg2Si alloy, Mater. Charact. 183 (2022) 111623, https://doi.org/10.1016/J.MATCHAR.2021.111623.

[17] C. Mallmann, F. Hannard, E. Ferrié, A. Simar, R. Daudin, P. Lhuissier, A. Pacureanu, M. Fivel, Unveiling the impact of the effective particles distribution on strengthening mechanisms: A multiscale characterization of Mg+Y2O3 nanocomposites, Mater. Sci. Eng. A 764 (2019) 138170, https://doi.org/10.1016/J.MSEA.2019.138170.

[18] L. Zhao, J.G. Santos Macías, L. Ding, H. Idrissi, A. Simar, Damage mechanisms in selective laser melted AlSi10Mg under as built and different post-treatment conditions, Mater. Sci. Eng. A 764 (2019) 138210, https://doi.org/10.1016/J.MSEA.2019.138210.

[19] J.G. Santos Macías, C. Elangeswaran, L. Zhao, B. Van Hooreweder, J. Adrien, E. Maire, J.Y. Buffière, W. Ludwig, P.J. Jacques, A. Simar, Ductilisation and fatigue life enhancement of selective laser melted AlSi10Mg by friction stir processing, Scr. Mater. 170 (2019) 124–128, https://doi.org/10.1016/J.SCRIPTAMAT.2019.05.044.

[20] M. Arseenko, F. Hannard, L. Ding, L. Zhao, E. Maire, J. Villanova, H. Idrissi, A. Simar, A new healing strategy for metals: Programmed damage and repair, Acta Mater. 238 (2022) 118241, https://doi.org/10.1016/J.ACTAMAT.2022.118241.

[21] J. Gheysen, A. Kashiwar, H. Idrissi, J. Villanova, A. Simar, Suppressing hydrogen blistering in a magnesium-rich healable laser powder bed fusion aluminum alloy

[22] B. Beausir, J.J. Fundenberger. Analysis Tools for Electron and X-ray diffraction, ATEX - software, Université de Lorraine – Metz, 2017 www.atex-software.eu.

[23] R. Kaibyshev, K. Shipilova, F. Musin, Y. Motohashi, Continuous dynamic recrystallization in an Al–Li–Mg–Sc alloy during equal-channel angular extrusion, Mater. Sci. Eng. A 396 (2005) 341–351, https://doi.org/10.1016/J.MSEA.2005.01.053.

[24] K. Matsuda, T. Naoi, Y. Uetani, T. Sato, A. Kamio, S. Ikeno, High resolution energy-filtering transmission electron microscopy for equilibrium β-phase in an Al-Mg-Si alloy, Scr. Mater. 41 (1999) 379–383, https://doi.org/10.1016/S1359-6462(99)00169-4.

[25] C. Phongphisutthinan, H. Tezuka, E. Kobayashi, T. Sato, Effects of ¢-Mg2Si precipitates on semi-solid microstructures of wrought AlMgSi based alloys produced by deformation-semi-solid-forming process, (2013). https://doi.org/10.2320/matertrans.M2012339.

[26] S.G. Shabestari, M. Ghanbari, Effect of plastic deformation and semisolid forming on iron–manganese rich intermetallics in Al–8Si–3Cu–4Fe–2Mn alloy, J. Alloys Compd. 508 (2010) 315–319, https://doi.org/10.1016/J.JALLCOM.2010.08.043.

[27] A. Bjurenstedt, S. Seifeddine, A.E.W. Jarfors, The effects of Fe-particles on the tensile properties of Al-Si-Cu alloys, Metals, 6 (2016) 314. https://doi.org/10.3390/MET6120314.

[28] W.H. Walton, Feret's statistical diameter as a measure of particle size, Nature, 162 (1948) 329–330. https://doi.org/10.1038/162329b0.

[29] R.C. Picu, D. Zhang, Atomistic study of pipe diffusion in Al–Mg alloys, Acta Mater. 52 (2004) 161–171, https://doi.org/10.1016/J.ACTAMAT.2003.09.002.

[30] A.D. Brailsford, H.B. Aaron, Growth of grain-boundary precipitates, J. Appl. Phys. 40 (2003) 1702, https://doi.org/10.1063/1.1657835.

[31] R. Goswami, P.S. Pao, S.B. Qadri, R.L. Holtz, Severe plastic deformation induced sensitization of cryo-milled nanocrystalline Al-7.5 Mg, Metall. Mater. Trans. A Phys. Metall. Mater. Sci. 45 (2014) 2894–2898, https://doi.org/10.1007/s11661-014-2227-z.

[32] X. Zhang, Y. Lv, B. Liu, X. Zhou, T. Zhang, Y. Gao, Z. Dong, J. Wang, J.O. Nilsson, The influence of room temperature storage on intergranular corrosion susceptibility of AA6082 Al-Mg-Si alloy, Corros. Commun. 3 (2021) 71–79, https://doi.org/10.1016/J.CORCOM.2021.09.004.

[33] A. Ardalanniya, S. Nourouzi, H. Jamshidi Aval, Fabrication of a laminated aluminium matrix composite using friction stir processing as a cladding method, Mater. Sci. Eng.: B 272 (2021) 115326, https://doi.org/10.1016/J.MSEB.2021.115326.

[34] M. Emamy, M. Khodadadi, A. Honarbakhsh Raouf, N. Nasiri, The influence of Ni addition and hot-extrusion on the microstructure and tensile properties of Al–15% Mg2Si composite, Mater. Design (1980-2015) 46 (2013) 381–390. https://doi.org/10.1016/J.MATDES.2012.10.005.

[35] X.C. Tong, A.K. Ghosh, Fabrication of in situ TiC reinforced aluminum matrix composites, J. Mater. Sci. 36 (2001) 4059–4069, https://doi.org/10.1023/A:1017946927566/METRICS.

[36] D. Lassance, D. Fabrègue, F. Delannay, T. Pardoen, Micromechanics of room and high temperature fracture in 6xxx Al alloys, Prog. Mater. Sci. 52 (2007) 62–129, https://doi.org/10.1016/J.PMATSCI.2006.06.001.

[37] B.Y. Pines, Diffusion and the mechanical properties of solids, Soviet Physics Uspekhi 5 (1962) 251–271, https://doi.org/10.1070/PU1962v005n02ABEH003410.

[38] R. Bullough, R.C. Newman, The kinetics of migration of point defects to dislocations, Rep. Prog. Phys. 33 (1970) 101–148, https://doi.org/10.1088/0034-4885/33/1/303.

[39] Z. Balogh, G. Schmitz, 5 - Diffusion in METALS AND ALLOYS, in: D.E. Laughlin, K. Hono (Eds.), Physical Metallurgy, Fifth Edition, Elsevier, Oxford, 2014, pp. 387–559, https://doi.org/10.1016/B978-0-444-53770-6.00005-8.

[40] N. Van Dijk, S. Van Der Zwaag, N. Van Dijk, S. Van Der Zwaag, Self-healing phenomena in metals, Adv. Mater. Interfaces 5 (2018) 1800226, https://doi.org/10.1002/ADMI.201800226.